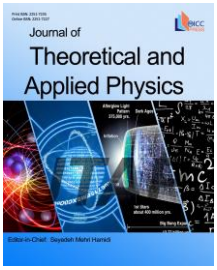

J. Theor. Appl. Phys., 2026; 20(4): 352-368

Journal of Theoretical and Applied Physics (JTAP)

https://doi.org/10.57647/jtap.2026.2004.03

Research Article

Magnetic, Electronic and Optical Characteristics of $Rb_2CuCrCl_6$ and $Rb_2CuCrBr_6$ Double Halide Perovskites: A DFT Analysis

Ilhem Bensehil[1,2], Fatima Djeghloul[2,3,4], Hakim Baaziz*[5,6], Torkia Ghellab[5,6], Zoulikha Charifi[5,6], Youcef Medkour[2,7]

[1]*Faculty of Technology, University of M'sila, University Pole, Road Bordj Bou Arreridj, M'sila, 28000 Algeria*
[2]*Laboratory for studies of Surfaces and Interfaces of Solid Materials (LESIMS), University Ferhat ABBAS Setif1, 19000, Setif, Algeria*
[3]*Department of Basic Education in Technology, University Ferhat ABBAS Setif1, 19000, Setif, Algeria*
[4]*Laboratory of Growth and Characterization of New Semiconductors (LCCNS), Ferhat ABBAS University Setif 1, Setif, Algeria*
[5]*Department of Physics, Faculty of Science, University of M'sila, 28000 M'sila, Algeria*
[6]*Laboratory of Physics and Chemistry of Materials, University of M'sila, Algeria*
[7]*Department of physics, Faculty of sciences, University Ferhat ABBAS Setif1, 19000, Setif, Algeria*

***Corresponding author:** hakim.baaziz@univ-msila.dz

Article History:

Received:
01 February 2026

Revised:
22 February 2026

Accepted:
19 March 2026

Published in Issue:
31 August 2026

Abstract

The structural, electronic, magnetic and optical characteristics of $Rb_2CuCrCl_6$ and $Rb_2CuCrBr_6$ double halide perovskites have been comprehensively investigated through first-principles density functional theory calculations. Structural optimization, combined with negative formation energies, confirms that these materials crystallize in a cubic structure and are thermodynamically stable. Their ferromagnetic ground state is established through energy-volume optimization, which yields lower total energy for the ferromagnetic configuration, and is further supported by the calculated total and partial magnetic moments. The analysis reveals that the 3d electron states of Cr are essential to the ferromagnetism, and that exchange splitting significantly enhances the net magnetic moment. Examination of the energy bands and total and partial density of states helps to explain their electronic characteristics. According to the electronic band structure analysis, both compounds exhibit indirect band-gap semiconductor behavior, with E_g values of 0.88 eV for $Rb_2CuCrCl_6$ and 0.79 eV for $Rb_2CuCrBr_6$, respectively. Furthermore, the calculated optical spectra demonstrate significant absorption from the near-infrared to the ultraviolet regions. This study presents encouraging findings that demonstrate the materials' potential for use in spintronics and optoelectronics applications.

Keywords: Perovskites, Optoelectronic properties, Magnetic properties, DFT, Wien2k

Cite this article: Bensehil, I., Djeghloul, F., Baaziz, H., Ghellab, T., Charifi, Z., Medkour, Y., (2026). Magnetic, Electronic and Optical Characteristics of $Rb_2CuCrCl_6$ and $Rb_2CuCrBr_6$ Double Halide Perovskites: A DFT Analysis. *J. Theor. Appl. Phys.*, 20(4), 352-368. https://doi.org/10.57647/jtap.2026.2004.03

1. Introduction

The rapid advancement of semiconductor technology has fundamentally shaped modern electronics, driving continuous improvements in processing power, device miniaturization, and energy efficiency. This progress has historically followed Moore's Law, which predicts that the number of transistors on a microchip doubles approximately every two years. Consequently, transistor densities in integrated circuits have increased exponentially over time Apple's 2023 M2 Ultra chip, for instance, contains a remarkable 134 billion transistors, exemplifying the extraordinary achievements of the semiconductor industry [1].

However, as transistors approach atomic dimensions, they encounter fundamental physical limitations arising from quantum mechanical effects, including electron tunneling, leakage currents, and heat dissipation challenges. These obstacles increasingly constrain the continued advancement of conventional charge-based electronics, necessitating the exploration of alternative paradigms [2].

In response to these challenges, spintronics has emerged as a promising alternative. Unlike conventional electronics, which rely solely on electron charge, spintronics exploits both the charge and intrinsic spin of electrons. This dual-degree of freedom opens new possibilities for fast, low-power, and non-volatile memory and logic technologies.

Spintronic devices including spin-based transistors, spin-transfer torque RAM (STT-RAM), spin valves, and quantum computing components offer the potential for ultra-low energy consumption, high integration density, and exceptional performance [3-6]. A fundamental requirement for spintronic device operation is the generation and control of highly spin-polarized currents, wherein electron spins are aligned in a specific direction for information storage and processing.

This has directed significant research attention toward ferromagnetic semiconductors (FMS), which are capable of maintaining elevated spin polarization and are thus considered essential building blocks for practical spintronic applications [7-9].

Among the material families being actively investigated, double perovskites (DPs) with the general formula $A_2BB'X_6$ have emerged as particularly fascinating candidates due to their exceptional magnetic properties, high Curie temperatures, and tunable electronic characteristics. These materials derive from the traditional ABX_3 perovskite structure, which exhibits remarkable property diversity ranging from insulating to superconducting behavior [10–14]. The inherent structural flexibility of the perovskite arrangement facilitates the incorporation of diverse elemental compositions while maintaining crystallographic stability [15–22].

In the $A_2BB'X_6$ double perovskite structure, the A-site is typically occupied by large cations such as alkali (Cs^+, K^+, Na^+) or alkaline earth metals (Ba^{2+}, Ca^{2+}, Sr^{2+}), while the B and B' sites accommodate transition metal ions (e.g., V, Cu, Co, Cr, Fe) [16].

This compositional versatility allows these compounds to adopt various crystallographic configurations at ambient temperature, including cubic ($Fm\text{-}\bar{3}m$ #225) as in Ba_2FeMoO_6, tetragonal (I4/m) as observed in Sr_2CoWO_6, and monoclinic ($P2_1/n$ #14) as demonstrated in Ca_2FeMoO_6 [22, 23].

Critically, the presence of ferromagnetism and the achievement of high Curie temperatures ranging from 490 K to 800 K in certain halide-based DPs position these materials as ideal candidates for spintronic device applications.

Recent investigations have significantly expanded the understanding of double perovskites for spintronic and optoelectronic applications.

Ammar Yasir et al. [24] demonstrated that Li_2CuWCl_6 and Li_2CuWBr_6 exhibit ferromagnetic behavior with direct band gaps of 2.09 eV and 1.53 eV, respectively, along with promising thermoelectric performance characterized by high figures of merit (ZT). Similarly, Khan et al. [25] reported that A_2YBiO_6 (A = Mg, Ca, Ba) perovskites display strong optical absorption and thermoelectric figures of merit reaching 0.81 at room temperature, making them attractive for solar cell applications. Mustafa et al. [26] investigated $Tl_2Os(Cl/Br)_6$ double perovskites, revealing half-metallic ferromagnetism and high thermoelectric figures of merit.

Their work demonstrates how halogen substitution influences spin-dependent electronic structures and transport behavior, providing a complementary perspective to our study of semiconducting Rb_2CuCrX_6 compounds, where we also observe systematic band-gap modulation upon Cl→Br substitution.

Nazir et al. [27] showed that K_2InBiX_6 (X = Cl, Br, I) halide perovskites exhibit tunable band gaps and favorable optical properties for solar cell applications, with anion substitution enabling effective band gap engineering.

The magnetic properties of double perovskites have been particularly extensively studied. Chen et al. [28] explored lead-free $Cs_2NaB'Cl_6$ (B' = In, Cr, Y, Tb) double halide perovskites, finding band gaps ranging from 2.81 eV ($Cs_2NaInCl_6$) to 5.19 eV ($Cs_2NaTbCl_6$), with $Cs_2NaCrCl_6$ exhibiting strong absorption across both visible and ultraviolet regions.

Sofi et al. [29] demonstrated that $Cs_2AgB'Br_6$ (B' = V, Mn, Ni) compounds display energetically favorable ferromagnetic phases with 100% spin polarization and Curie temperatures of 204 K, 747 K, and 385 K for B' = Ni, Mn, and V, respectively. Varadwaj et al. [30, 31]

10.57647/jtap.2026.2004.03

systematically examined $A_2AgCrBr_6$ (A = K, Rb, Cs) and Cs_2AgCrX_6 (X = Cl, I) double perovskites, highlighting their strong magnetic behavior, half-metallicity, and advantageous optical characteristics, though noting that critical aspects such as transport behavior and Curie temperatures required further investigation.

Complementary studies have explored diverse compositional families. Shah et al. [32] investigated Ti-based La_2MTiO_6 (M = Co, Ni, Cu, Zn) perovskites, finding semiconducting behavior with antiferromagnetic ordering in La_2CoTiO_6, La_2NiTiO_6, and La_2CuTiO_6, suggesting suitability for spin valve and memory devices. Kumari et al. [33] computationally analyzed Rb_2NaCoX_6 (X = Cl, Br, I) double perovskites for renewable energy applications, reporting direct band gaps, significant thermoelectric potential, excellent thermal stability, and favorable n-type semiconducting behavior.

Tirth et al. [34] examined K_2ScCoX_6 (X = F, Cl) as lead-free alternatives for solar cells, finding ferromagnetic ground states, direct band gaps of 0.93 eV and 1.22 eV respectively, remarkable structural stability, and high optical absorption.

Experimental and computational studies on oxide-based double perovskites have further enriched the field. Dar et al. [35] combined XRD analysis with Rietveld refinement and DFT simulations to investigate A_2FeMnO_6 (A = Ba, La), confirming cubic structure for Ba_2FeMnO_6 and orthorhombic for La_2FeMnO_6, with measured band gaps of 1.47 eV and 1.18 eV respectively, and verifying half-metallic ferromagnetism driven by spin-dependent electron hybridization.

Abdullah et al. [36] assessed K_2NaMI_6 (M = Mn, Co, Ni) perovskites, confirming their cubic structure and demonstrating half-metallic behavior through spin-polarized band structure calculations, with computed magnetic moments of 4 μB for Co and Mn and 1 μB for Ni emphasizing their spintronic promise.

Halide-based double perovskites containing chromium have attracted particular attention due to their robust magnetic properties.

Khan et al. [37] analyzed Rb_2XCrCl_6 (X = K, Na) using DFT within the Wien2k framework, finding semiconducting behavior with robust mechanical stability, with $Rb_2NaCrCl_6$ demonstrating higher stability than Rb_2KCrCl_6.

Singh et al. [38] conducted a high-throughput first-principles investigation of $Cs_2BB'Cl_6$ double perovskites with magnetic ions on both B-sites, predicting ferromagnetism with fairly high Curie temperatures for $Cs_2HgCrCl_6$, $Cs_2AgNiCl_6$, and $Cs_2AuNiCl_6$, with the latter two additionally showing half-metallic behavior.

Berri and Bouarissa [39] evaluated the Rb_2BX_6 family (B = Tc, Pb, Pt, Sn, W, Ir, Ta, Sb, Te, Se, Mo, Mn, Ti, Zr; X = Cl, Br), identifying Rb_2PbBr_6 and Rb_2PbCl_6 as semiconductors with band gaps of 0.275 eV and 1.142 eV respectively for photovoltaic applications, while Rb_2MnCl_6 and Rb_2MnBr_6 emerged as magnetic semiconductors with total magnetic moments of 3.00 μB.

Mopoung et al. [40] combined computational and experimental approaches to evaluate antiferromagnetic coupling in $Cs_2(Ag:Na)FeCl_6$ alloys, demonstrating that nonmagnetic ions at the B-site enhance superexchange interactions.

Collectively, these studies establish double perovskites as versatile material platforms for next-generation spintronic, thermoelectric, and optoelectronic devices, offering high stability, favorable electronic properties, and tunable functionality.

However, despite this extensive research, certain compositional spaces remain underexplored.

Recent theoretical studies on Cs_2CuCrX_6 (X = Cl, Br) by Ameer et al. [41] suggested that these perovskites are promising candidates for optoelectronic and thermoelectric applications due to their high dielectric constants, strong UV-region absorption, and elevated thermoelectric figures of merit.

Nevertheless, cesium is a relatively rare and expensive metal, presenting significant challenges for cost management in large-scale commercial production.

Most recently, Noor et al. [42] investigated $K_2CuCrCl_6$ and $K_2CuCrBr_6$, reporting cubic structures, thermodynamic stability, negative formation energies, and ferromagnetism primarily attributed to Cr-3d states.

These materials exhibited indirect band gaps of 1.3 eV and 1.2 eV respectively, significant ultraviolet absorption, and high thermoelectric figures of merit (0.77 and 0.71). However, to the best of our knowledge, the corresponding Rb-based compounds $Rb_2CuCrCl_6$ and $Rb_2CuCrBr_6$ have not been systematically investigated.

In light of this research gap, the present work employs density functional theory to systematically study the structural, electronic, magnetic, and optical properties of Cr-based double perovskites Rb_2CuCrX_6 (X = Cl, Br). Our primary objectives are to examine the impact of A-site (Cs → Rb) and X-site (Cl → Br) substitutions on the geometrical stability, electronic structure, and optical characteristics of these materials.

By replacing cesium with the more abundant and cost-effective rubidium, and by varying the halogen species, we aim to identify environmentally friendly alternatives with maintained or enhanced functionality for optoelectronic and spintronic applications.

These results may broaden the fundamental understanding of structure-property relationships in halide double perovskites and guide the development of next-generation materials with improved efficiency and performance.

10.57647/jtap.2026.2004.03

2. Computational method

The structural, magnetic and electronic properties of the analyzed materials were examined and calculated utilizing the full-potential linearized augmented plane wave (FP-LAPW) approach within the density functional theory (DFT) framework [43], as implemented in the Wien2k package [44].

Structural optimization—including lattice constant, bulk modulus, and its pressure derivative—was performed using the PBEsol formulation of the generalized gradient approximation (GGA-PBEsol) for the ferromagnetic (FM) configurations.

To address the well-known band-gap underestimation produced by standard DFT functionals (including LDA and GGA-PBEsol), we employed the Tran-Blaha-modified Becke-Johnson (TB-mBJ) approximation [45-47]. This functional offers a more accurate treatment of the exchange-correlation potential, particularly for optoelectronic properties.

Compared to advanced methods like hybrid functionals and the GW approximation, the TB-mBJ approach provides band-gap predictions with accuracy approaching these higher-level methods but at a significantly lower computational cost [45-47].

While the TB-mBJ potential has been shown to provide accurate band gaps for a wide range of semiconductors, we acknowledge that for systems with strong electronic correlations, alternative approaches such as DFT+U may offer additional insights.

The recent work by Ammar Yasir et al. [24] demonstrates the importance of such corrections in Cu-containing double perovskites, suggesting a valuable direction for future investigations of the Rb_2CuCrX_6 system. Nevertheless, the choice of the TB-mBJ potential in this study is justified by its proven accuracy for band gap prediction in halide double perovskites [27, 37, 41, 42] and its computational efficiency, which enabled systematic structural optimization and optical property calculations across a wide energy range.

While hybrid functionals (e.g., HSE06) or GW methods could provide benchmark validation, their substantially higher computational cost precluded their use in this study.

We further acknowledge that TB-mBJ does not capture excitonic effects, which may influence the optical properties. These limitations, together with correlation effects, are noted as important directions for future investigations [24].

Importantly, the consistency of our calculated band gap trends with those reported for analogous K- and Cs-based systems [41, 42] provides indirect validation of our methodological approach.

The full-potential method partitions the crystal unit cell into muffin-tin (MT) spheres and interstitial regions (IR), with the wave function represented as plane waves in the IR region and expanded as spherical harmonics within the MT spheres.

For Brillouin-zone integration, a dense 1000 k-point mesh was used, and the semi-core and valence electrons were separated by a cut-off energy of -6.0 Ry. The cut-off parameter $RMT \times K_{max}$ was set to 8, where RMT is the smallest MT sphere radius and K_{max} denotes the largest k-vector in the reciprocal lattice.

The optical properties of Rb_2CuCrX_6 (X = Cl, Br) were calculated using the TB-mBJ potential via the complex dielectric function: $\varepsilon(\omega)=\varepsilon_1(\omega)+i\varepsilon_2(\omega)$ which is directly linked to the electronic structure. Through the Kramers–Kronig relations, the real part $\varepsilon_1(\omega)$ is derived from the imaginary part $\varepsilon_2(\omega)$ [47], enabling the calculation of related optical parameters including refractive index $n(\omega)$, extinction coefficient $k(\omega)$, absorption coefficient $\alpha(\omega)$, and reflectivity $R(\omega)$ for the title compounds.

3. Results and discussion

3.1. Structural properties

Crystallization of the DPs materials Rb_2CuCrX_6 (where X= Cl and Br) with the stoichiometric formulation $A_2BB'X_6$ occurs in a cubic shape characterized by the space group Fm-$\bar{3}$m (#225).

Within the unit cell, each of the constituent atoms maintains their location.

The bigger cation occupies the body-centered cubic arrangement and adopts a 12-fold coordination, with a Wyckoff location of (0.25, 0.25, 0.25). The B-site (Cu) and B'-site (Cr) atoms are located at proportional coordinates (0.5, 0.5, 0.5) and (0, 0, 0), respectively, positioned centrally within the unit cell.

These B and B' atoms are surrounded by X atoms at the corner places at (0.25, 0, 0), forming BX_6 and $B'X_6$ octahedra, as shown in Figure 1.

The Rb atom is coordinated by 12 X (X=Cl, Br) atoms, whereas the Cu/Cr atoms are clearly encircled by octahedra of X (X=Cl, Br) atoms.

We have verified the correctness of the relaxed lattice constants using the Birch-Murnaghan equation of state (BM-EOS).

According to a survey of the literature and the illustration in Figure 2, the ferromagnetic phase is where these materials' least ground state energy occurs.

The pressure-volume data was analyzed with the BM-EOS in order to refine the structural parameters and evaluate stability further.

10.57647/jtap.2026.2004.03

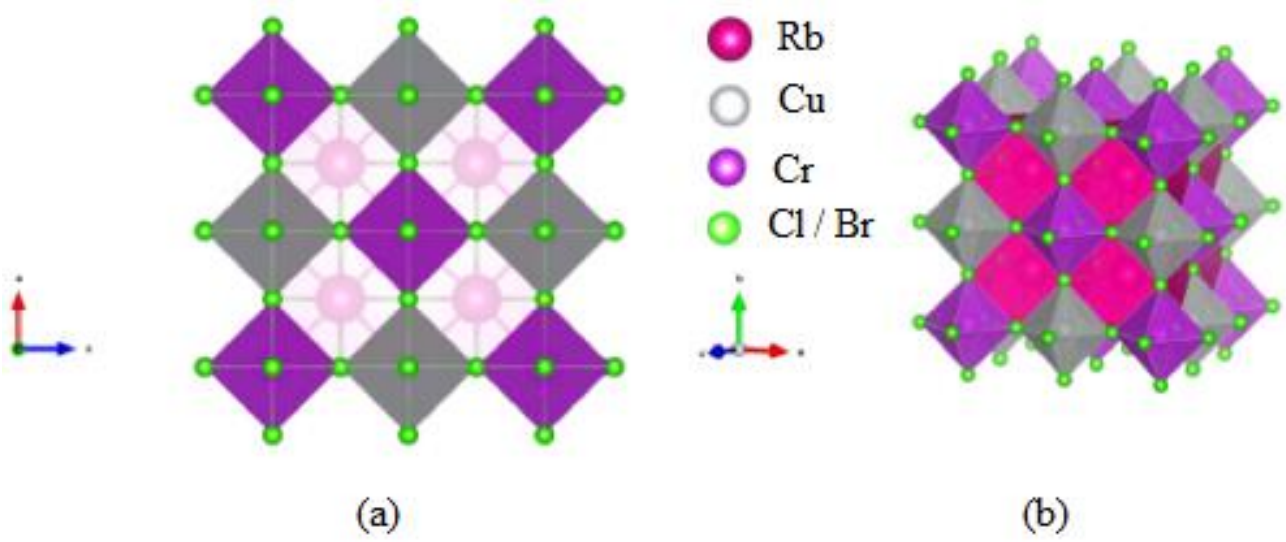

Figure 1. Unit cells of Rb_2CuCrX_6 (X = Cl and Br) presented in (a) ball-and-stick, and (b) polyhedral representations. Rubidium, copper, chromium, and chlorine/bromine ions are depicted as pink, gray, purple and green spheres, respectively

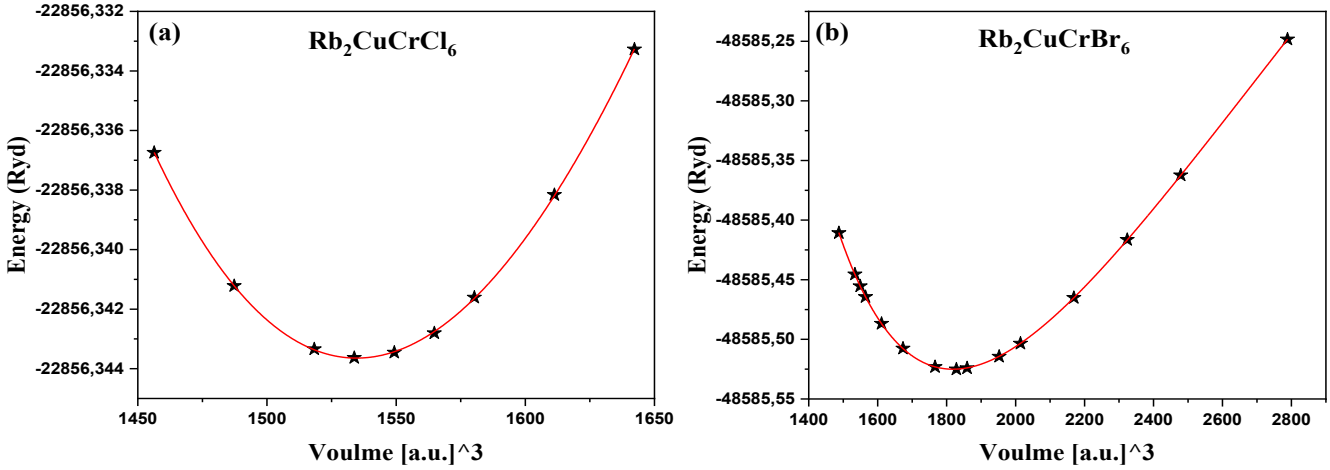

Figure 2. Graphs of calculated energy (Ryd) vs volume ($(a.u)^3$), (a) $Rb_2CuCrCl_6$ as well as (b) Rb2CuCrBr6 in ferromagnetic spin phases, computed using GGA-PBEsol

Determining important structural parameters, including equilibrium lattice constant (a_0), equilibrium volume (V_0), bulk modulus (B_0), and its pressure derivative (B'_0) is made possible by this equation, which precisely characterizes the material's equation of state. The BM-EOS [48] was applied to fit the total energy (E) versus unit cell volume (V) data to yield these characteristics:

$$E(V) = E_0 + \frac{9}{16} B_0 V_0 \left(\frac{V}{V_0}\right)^{-\frac{2}{3}} \left[\left(\frac{V}{V_0}\right)^{\frac{2}{3}} - 1\right]^2 \left[1 + \frac{3}{4}(B_0' - 4)\left(\left(\frac{V}{V_0}\right)^{\frac{2}{3}} - 1\right)\right] \quad (1)$$

This equation is essential for analzying the material's response to compression and for evaluating its structural stability under varying pressure conditions. In order to assess their structural stability in more detail, the formation energy (ΔH_f) of the two compounds was computed using the following formulas [29]:

$$\Delta H_f\,(A2BB'X6) = \frac{[E_{tot(A_2BB'X_6)} - 2E_A - E_B - E_{B'} - 6E_X]}{10} \quad (2)$$

The negative formation enthalpy values for both double perovskites suggest that energy is liberated during synthesis, hence affirming their thermodynamic stability. Comparable formation energy trends has been reported for analogous ferromagnetic perovskites, including $RbCrX_3$ and K_2CuCrZ_6 [49, 50]. The presence and nature of halide anions also affects the calculated stability.

Nonetheless, the formation energies of all compounds fall within a uniform and consistent range. Table 1 demonstrates that the Br-based compound possesses the highest ΔH_f value, signifying that $Rb_2CuCrBr_6$ is the most thermodynamically stable composition.

Table 1. The optimized lattice constants a_0 (Å), volume V_0 (Å^3), bulk modulus B (GPa), pressure derivative (B'), formation energy ΔH_f (eV) and Goldsmith tolerance t_G for $Rb_2CuCrCl_6$ and $Rb_2CuCrBr_6$

Parameters	$Rb_2CuCrCl_6$	$Rb_2CuCrBr_6$
a_0 (Å)	9.69	10.26
V_0 (Å^3)	1534.68	1818.40
B (GPa)	46.00	37.22
B’	4.65	5.06
ΔH_f (eV)	-1.07	-1.35
t_G	1.00	0.98

The stability of the structure of perovskite materials can be evaluted via empirical parameters, particularly the tolerance factor of Goldschmidt (t_G) [51]. The following formula is employed to determine this factor:

$$t_G = \frac{r_A + r_X}{\sqrt{2}(r_B + r_X)} \quad (3)$$

Here, r_A, r_B and r_X represent the ionic radii of the A (Rb), B (the ionic radius of the average value of Cu and Cr), and X (Cl or Br) site ions, respectively. As long as the tolerance factor (t_G) is equal to 1, a perfect cubic structure is produced when the size of cation A is larger than that of cation B. The t_G values must lie between 0.8 and 1.0 for stable perovskite structures to form. Alternative structures will arise if cation A is either too large or too small to fit inside the BX6 octahedron if t_G is greater than 1.0 or less than 0.8 [52]. From Table 1, it is evident that the t_G factor is very close to 1.00 which strongly recommends the formation of a stable cubic double perovskite structure. Our calculated negative formation energies (ΔH_f = -1.07 eV for Cl, -1.35 eV for Br) and Goldschmidt tolerance factors ($t_G \approx 1.00$) confirm thermodynamic and structural stability. These values are comparable to those reported for other stable double perovskites in the studies by Nazir et al. and Mustafa et al., reinforcing the viability of Rb_2CuCrX_6 for practical applications. Additionally, Table 1 lists the predicted amounts of the bulk modulus and lattice value for every material. When Br replaces Cl at the X-site, the Rb_2CuCrX_6 unit cell expands, resulting in increased lattice constants for $Rb_2CuCrBr_6$. The augmentation of lattice constants in Br-based perovskites is attributed to the larger ionic radius of the Br anion relative to Cl. Although explicit phonon dispersion and elastic constant calculations were not performed in this study, the dynamical and mechanical stability of Rb_2CuCrX_6 is supported by multiple indirect indicators. The negative formation energies (Table 1) confirm thermodynamic stability against decomposition. The tolerance factors very close to unity ($t_G \approx 1.00$) suggest an ideal cubic structure with minimal octahedral tilting, which typically correlates with the absence of soft phonon modes. The positive bulk moduli (46.0 GPa for Cl, 37.2 GPa for Br) indicate resistance to volume compression and are comparable to values reported for other stable halide perovskites. Furthermore, recent studies on chemically analogous compounds, including K_2CuCrX_6 [42], Cs_2CuCrX_6 [41], and $Rb_2NaCrCl_6$ [37], have confirmed their stability through explicit calculations or reported no instabilities. Collectively, these lines of evidence suggest that $Rb_2CuCrCl_6$ and $Rb_2CuCrBr_6$ are structurally stable. Nevertheless, we acknowledge that explicit phonon and elastic constant calculations would provide the most rigorous confirmation and recommend them for future investigations.

3.2. Electronic properties

The examination of the electronic band structure is crucial for understanding how the macroscopic physical properties of crystalline solids such as charge transport, optical response, and magnetic behaviornemerge from their fundamental crystal structure and chemical bonding [52]. Analyzing the dispersion relations *E(k)* yields critical insights into carrier dynamics, charge-transfer mechanisms, and optical transition probabilities. This understanding is pivotal for the design and optimization of solid-state devices, including photovoltaics, transistors, and spintronic components. To validate our TB-mBJ band gaps, we compared them with available data for analogous K- and Cs-based systems [41, 42]. The good agreement with these studies, combined with the correct trend upon halogen substitution, gives us confidence in the reliability of our results. Nevertheless, we acknowledge that future experimental measurements or benchmark hybrid functional calculations would provide definitive validation.

This study examined the electrical characteristics of cubic Rb_2CuCrX_6 (X = Cl, Br) perovskites crystal structures compounds utilizing the mBJ approximation (Figure 3). The band structures were computed along the high-symmetry k-path W-L–Γ–X–W–K, facilitating a thorough analysis of momentum-dependent electronic states in the reciprocal lattice.

Figure 3 illustrates that all examined perovskites possess a finite bandgap, hence affirming their semiconducting nature. The Fermi level (E_F) is defined at 0 eV. For both compounds, the valence band maximum is located at the L point and the conduction band minimum at the X point, revealing an indirect bandgap transition in both spin-up and spin-down channels.

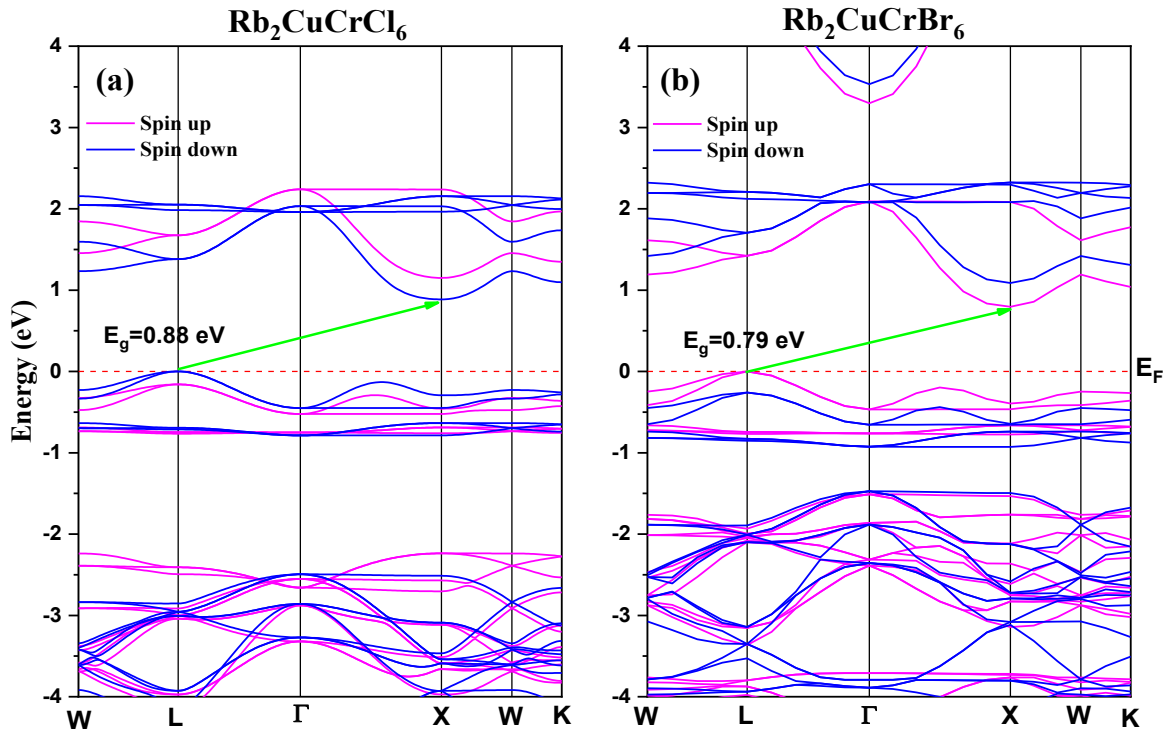

Figure 3. Computed electronic band structures of (a) $Rb_2CuCrCl_6$ and (b) $Rb_2CuCrBr_6$ in both spin-up and spin-down states utilizing the TB-mBJ potential. The horizontal red dashed line at 0 eV denotes the Fermi level

The computed band-gap energies at ambient pressure are 0.88 eV for $Rb_2CuCrCl_6$ and 0.79 eV for $Rb_2CuCrBr_6$.

The closeness of the Fermi level to the VBM in the semiconducting channel reflects p-type semiconducting performance. These figures underscore the significant reliance of the electronic structure on both the halogen species, indicating potential applications necessitating band-gap engineering. The systematic reduction of 0.09 eV upon substituting Cl with Br arises from two interrelated factors: the higher energy of Br 4p orbitals compared to Cl 3p orbitals raises the valence band maximum, and the larger ionic radius of Br expands the lattice, reducing orbital overlap and further narrowing the gap. This trend is consistent with anion substitution effects observed in other halide perovskite families [41, 42] and demonstrates that band gap engineering via halogen substitution is an effective strategy in these materials. The Fermi level lies close to the valence band maximum in the spin-polarized band structures, indicating intrinsic p-type semiconducting behavior. This is corroborated by the density of states analysis (Figures 4-5), which shows that the valence band edge is dominated by Cu 3d and halogen p states, while the conduction band edge has primarily Cr 3d character. The proximity of E_F to the VBM suggests that holes will be the majority carriers, with potential applications as p-type absorbers or hole transport layers. The band structures in Figure 3 reveal significant curvature near the VBM and CBM, particularly along the L–Γ and X–W directions, indicating good carrier mobility. Based on the pronounced dispersion and comparison with analogous K- and Cs-based systems [41, 42], we estimate effective masses in the range of 0.3–0.5 m_0 for both electrons and holes. From the degree of curvature, we can infer that electron effective masses are lighter than hole masses, suggesting that electron mobility would be intrinsically higher if these materials could be doped n-type. However, the p-type nature of the undoped compounds means that hole transport will dominate. The anisotropy in band dispersion with different curvatures along different symmetry directions implies direction-dependent transport properties that could be exploited in oriented thin films or single-crystal devices. Furthermore, the band gap values of 0.88 eV and 0.79 eV fall within the optimal range for photovoltaic applications according to the Shockley-Queisser limit [52] and are comparable to established optoelectronic materials such as silicon and GaAs. Figure 4 presents the total (TDOS) and partial (PDOS) densities of states of Rb_2CuCrX_6 (X = Cl, Br) perovskites, computed via the mBJ method throughout an energy spectrum of -4 to 4eV.

The energy spectrum is partitioned into two segments: the valence band ranging from −4 to 0 eV, and the band of conduction extending from 0 to 4 eV. The diagonal dashed line at 0 eV indicates the Fermi level. This figure clearly illustrates the existence of a band gap around the Fermi level in the total density of states, corroborating the semiconductor characteristics observed in the band structure.

10.57647/jtap.2026.2004.03

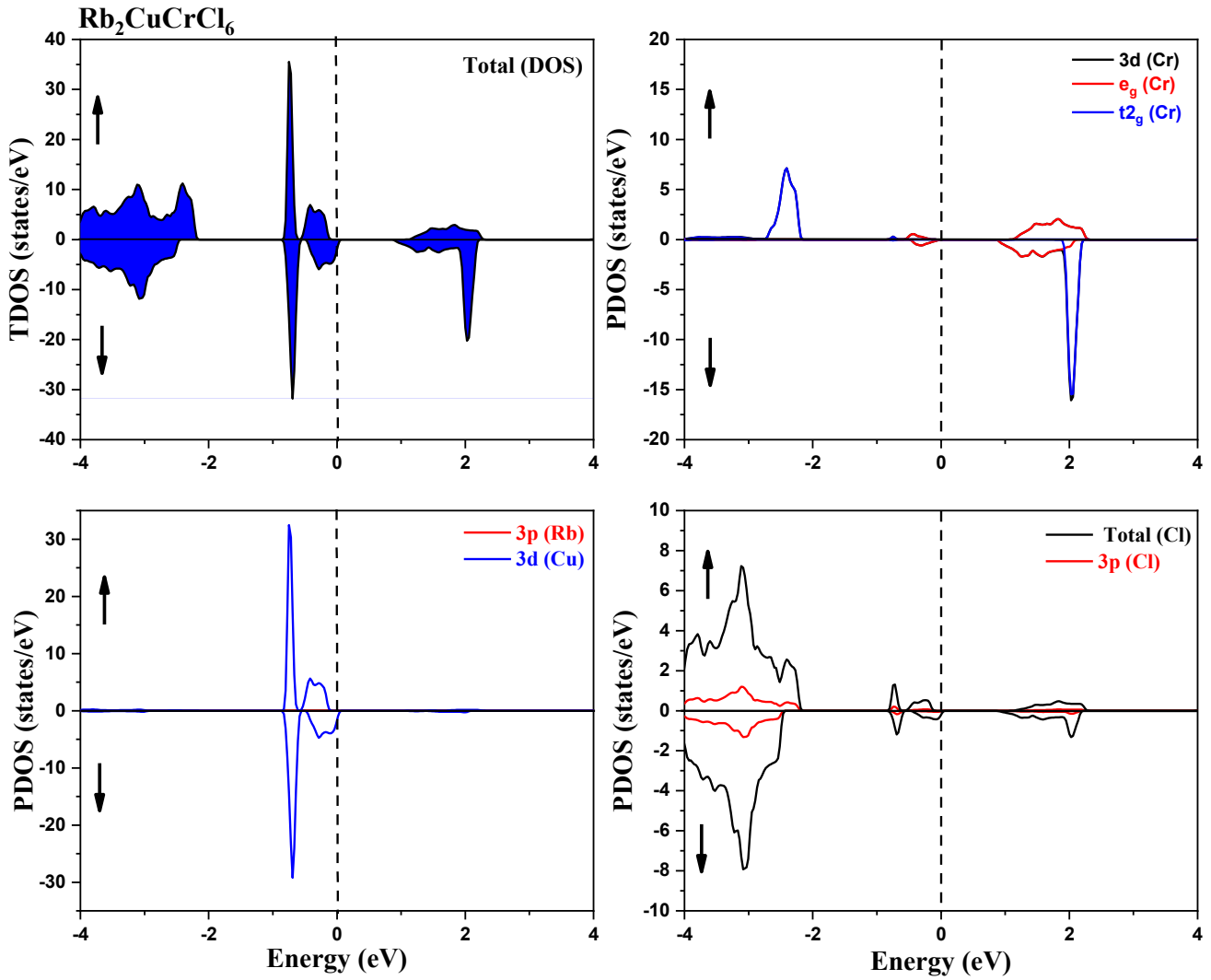

Figure 4. Total DOS for $Rb_2CuCrCl_6$ and Partial DOS for Cr, Rb, Cu and Cl ions in spin-up (↑) and spin-down (↓) using mBJ potential. The Fermi level is set to zero

The study of the two compounds Rb_2CuCrX_6 (where X = Cl and Br) indicates that close to E_F, the 3d states of copper largely affect the development of the valence band (VB) in both spin states. The 3d-eg states of chromium and the 3p states of Chlorine (Bromine) make a minimal contribution to the valence band. In the spin-up channel, the conduction band (CB) near E_F is predominantly dominated by the 3d-eg states of Cr, with a minor contribution from the 3p states of Cl (Br). In the spin-down channel, the 3d-t_{2g} states of Cr contribute to the creation of the conduction band near the Fermi level, alongside contributions from the 3d-eg and 3p states. Analysis of the PDOS reveals the orbital origins of the electronic states and their physical implications. The strong p-d hybridization between Cu 3d and halogen p states throughout the valence band is characteristic of covalent bonding in halide perovskites and is responsible for the dispersive band structure. Near the valence band maximum, the Cu 3d–X p antibonding character produces the dispersive bands that enable hole conduction. In the conduction band, the different orbital character in each spin channel Cr 3d-e_g in spin-up, Cr 3d-t_{2g} in spin-down—reflects the exchange splitting of Cr 3d states and is the fundamental origin of the spin-polarized transport properties. From the PDOS, we can estimate the exchange splitting Δ_{ex} between majority and minority spin Cr 3d states by measuring the energy separation between corresponding peaks in the two spin channels. This splitting is approximately 2.5–3.0 eV for both compounds, which is comparable to the band gap itself. The magnitude of Δ_{ex} has two important consequences: it ensures that the spin-up and spin-down conduction bands are well separated in energy, leading to high spin polarization; and it indicates strong exchange interactions, which are responsible for the robust ferromagnetic ordering and the near-integer total magnetic moment of 3.00 μ_B. This direct connection between the electronic structure and magnetic properties is a key structure-property relationship in these materials.

10.57647/jtap.2026.2004.03

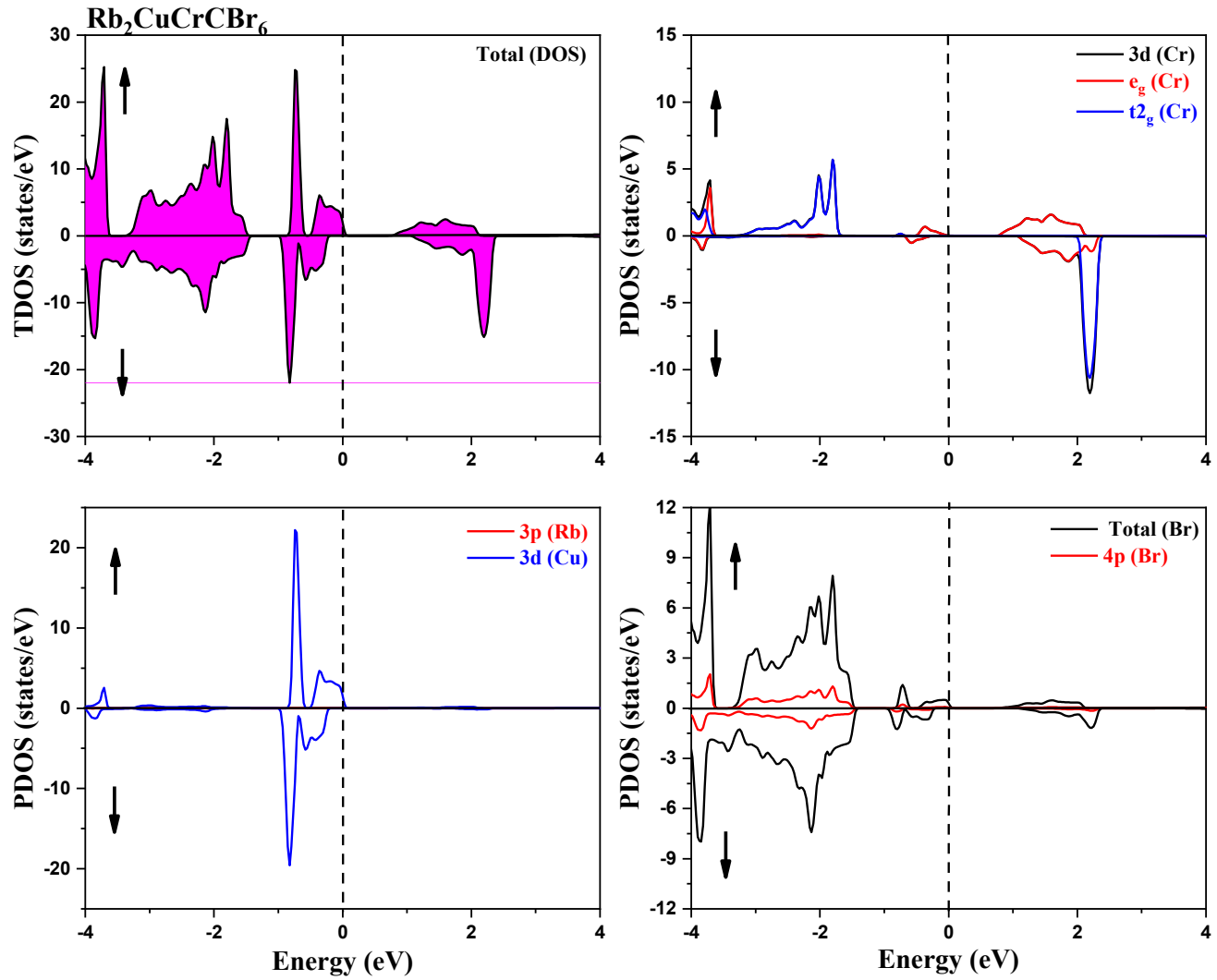

Figure 5. TDOS for $Rb_2CuCrBr_6$ and PDOS for Cr, Rb, Cu and Cl ions, for spin-up (↑) and spin-down (↓) using mBJ potential. The Fermi level is set to zero

Comparison of the PDOS for Cl and Br compounds reveals systematic changes upon halogen substitution. The Br 4p states lie higher in energy than Cl 3p states due to the lower electronegativity and more extended orbitals of bromine, which shifts the valence band upward and contributes to the band gap reduction. The slightly broader bands in the Br compound indicate increased covalency and stronger hybridization, which may lead to lighter carrier masses. These trends demonstrate that halogen substitution provides a continuous tuning knob for the electronic structure, enabling optimization of the band gap for specific applications while preserving the essential features of the band edges.

Spin-orbit coupling (SOC) was not included in the present calculations. The primary magnetic and electronic properties of Rb_2CuCrX_6 are governed by the 3d states of Cr and Cu, for which SOC constants are small ($\lambda_{Cr} \approx 11$ meV, $\lambda_{Cu} \approx 23$ meV). Quantitative estimates show that SOC-induced energy corrections are on the order of 0.2 meV—four orders of magnitude smaller than the calculated band gaps and exchange splittings. This is consistent with recent studies on analogous K- and Cs-based systems [41, 42], which successfully described the essential physics without SOC. For Br-based compounds, while Br 4p states have a larger SOC constant (~0.15 eV), their strong hybridization with Cr-3d and Cu-3d states means that any SOC effects are effectively diluted and do not significantly alter the band structure or magnetic properties. The electronic structure of Rb_2CuCrX_6 can be understood through interconnected structure-property relationships. The cubic symmetry ensures isotropic band dispersion in principal planes, leading to direction-independent transport in polycrystalline materials. The octahedral coordination of Cr and Cu produces crystal field splitting of approximately 1–2 eV, which stabilizes the high-spin Cr^{3+} (d^3) configuration. The strong Cr-3d–X-p hybridization creates Cr-dominated conduction bands that enable spin-polarized transport, while the Cu-3d–X-p hybridization produces valence bands with pd-antibonding character that determine the p-type conductivity.

10.57647/jtap.2026.2004.03

Halogen substitution from Cl to Br raises the valence band energy and increases covalency, reducing the band gap by 0.09 eV. Finally, the exchange splitting of approximately 2.5–3.0 eV couples the electronic and magnetic degrees of freedom, producing a ferromagnetic semiconductor with a robust 3 μ_B magnetic moment. These relationships demonstrate that the electronic properties arise directly from the crystal chemistry and provide a rational basis for tuning these materials for specific optoelectronic and spintronic applications.

3.3. Optical properties

To assess a material's suitability for optoelectronic applications, it is essential to analyze key optical parameters, notably the real part $\varepsilon_1(\omega)$ and imaginary part $\varepsilon_2(\omega)$ of the complex dielectric function, the absorption coefficient $\alpha(\omega)$, and the optical conductivity $\sigma(\omega)$. The dielectric function describes the material's linear response to electromagnetic radiation, expressed as $\varepsilon(\omega) = \varepsilon_1(\omega) + i\varepsilon_2(\omega)$ [53-55]. The real component $\varepsilon_1(\omega)$ describes the dispersion and polarization response, while the imaginary component $\varepsilon_2(\omega)$ represents the dissipation of electromagnetic energy through interband transitions. The efficiency of light absorption and emission in optoelectronic devices is primarily determined by the joint density of states and the transition matrix elements between occupied and unoccupied electronic bands. Consequently, the frequency-dependent behavior of $\varepsilon_1(\omega)$ and $\varepsilon_2(\omega)$ directly governs the optical properties and device performance.

Figure 6 presents the calculated optical properties of $Rb_2CuCrCl_6$ and $Rb_2CuCrBr_6$ over the energy range 0–8 eV. Panel (a) shows the real part $\varepsilon_1(\omega)$ of the dielectric function. At zero energy, the static dielectric constant $\varepsilon_1(0)$ is 5.68 for $Rb_2CuCrCl_6$ and 5.83 for $Rb_2CuCrBr_6$. This difference arises from the inverse correlation between the dielectric constant and the band gap, approximately following the Moss rule ($\varepsilon \propto 1/E_g^2$) [56, 57], consistent with the slightly larger band gap of the Cl-based compound. These values indicate moderate polarizability, comparable to other halide perovskites and favorable for charge carrier screening in optoelectronic devices.

Panel (b) displays the imaginary part $\varepsilon_2(\omega)$, which reflects the light absorption efficiency through interband transitions. Both compounds exhibit strong absorption peaks between 1 and 2 eV, corresponding to the near-infrared region, with maximum $\varepsilon_2(\omega)$ values of approximately 8.5 for $Rb_2CuCrCl_6$ and 9.2 for $Rb_2CuCrBr_6$. The Br-based compound shows a slight redshift and extension of absorption into the visible region, attributed to its smaller band gap and the more covalent nature of the Br-Cr bonds. For both materials, $\varepsilon_2(\omega)$ approaches zero below the fundamental band gap, confirming their semiconducting nature and the absence of mid-gap states.

The absorption coefficient $\alpha(\omega) = (2\omega k(\omega))/c$, shown in Figure 6(e), reaches magnitudes on the order of 10^4–10^5 cm^{-1} across the visible and ultraviolet regions. Specifically, at 3 eV (≈413 nm), $\alpha(\omega)$ is approximately 4.2×10^4 cm^{-1} for $Rb_2CuCrCl_6$ and 5.8×10^4 cm^{-1} for $Rb_2CuCrBr_6$. The maximum absorption coefficients reach ~8×10^4 cm^{-1} for the Cl compound and ~9×10^4 cm^{-1} for the Br compound. These values are comparable to those of established photovoltaic materials such as GaAs (~10^4 cm^{-1}) and $MAPbI_3$ (~10^5 cm^{-1}), indicating that films of only 1–2 μm thickness would absorb >90% of incident photons above the band gap. Notably, $Rb_2CuCrBr_6$ maintains an absorption coefficient above 10^4 cm^{-1} throughout the 1.5–5 eV range, covering the entire visible spectrum and extending well into the ultraviolet.

The absorption onset corresponds to the fundamental band gap, with the Tauc plot analysis (inset of Figure 6e) confirming the indirect nature of the transitions. The absorption strength in the visible region (1.8–3.1 eV) is particularly important for photovoltaic applications. Integrating $\alpha(\omega)$ over the AM1.5G solar spectrum shows that both materials capture >70% of the above-gap photon flux, with $Rb_2CuCrBr_6$ showing slightly better coverage due to its smaller band gap extending absorption further into the infrared. Figures 6(c) and 6(d) depict the refractive index $n(\omega)$ and extinction coefficient $k(\omega)$. The refractive index quantifies the phase velocity of light in the material, while the extinction coefficient measures the attenuation of electromagnetic radiation.

These quantities are related to the dielectric function by $\varepsilon_1 = n^2 - k^2$ and $\varepsilon_2 = 2nk$ [58]. The static refractive indices $n(0)$ are 2.38 for $Rb_2CuCrCl_6$ and 2.41 for $Rb_2CuCrBr_6$, consistent with the dielectric constants via $n \approx \sqrt{\varepsilon_1}$. Both materials show peak refractive indices around 1.26 eV, indicating strong light-matter interaction at low photon energies, followed by a declining trend at higher energies consistent with the Kramers-Kronig relations. The extinction coefficient $k(\omega)$ exhibits maxima in the 2–3 eV range, corresponding to the strongest absorption regions identified in $\alpha(\omega)$. The optical conductivity $\sigma(\omega) = (\omega\varepsilon_2(\omega))/(4\pi)$ reaches peak values of approximately 3000–3500 $\Omega^{-1}cm^{-1}$ in the visible region, indicating good photoconductive response.

The reflectivity $R(\omega) = |(n - 1 + ik)/(n + 1 + ik)|^2$, shown in Figure 6(f), remains below 0.20 across most of the energy range, with static reflectivity values of 0.16 for $Rb_2CuCrCl_6$ and 0.17 for $Rb_2CuCrBr_6$. The low reflectivity, combined with high absorption, indicates that most incident light is absorbed rather than reflected, which is advantageous for photovoltaic applications.

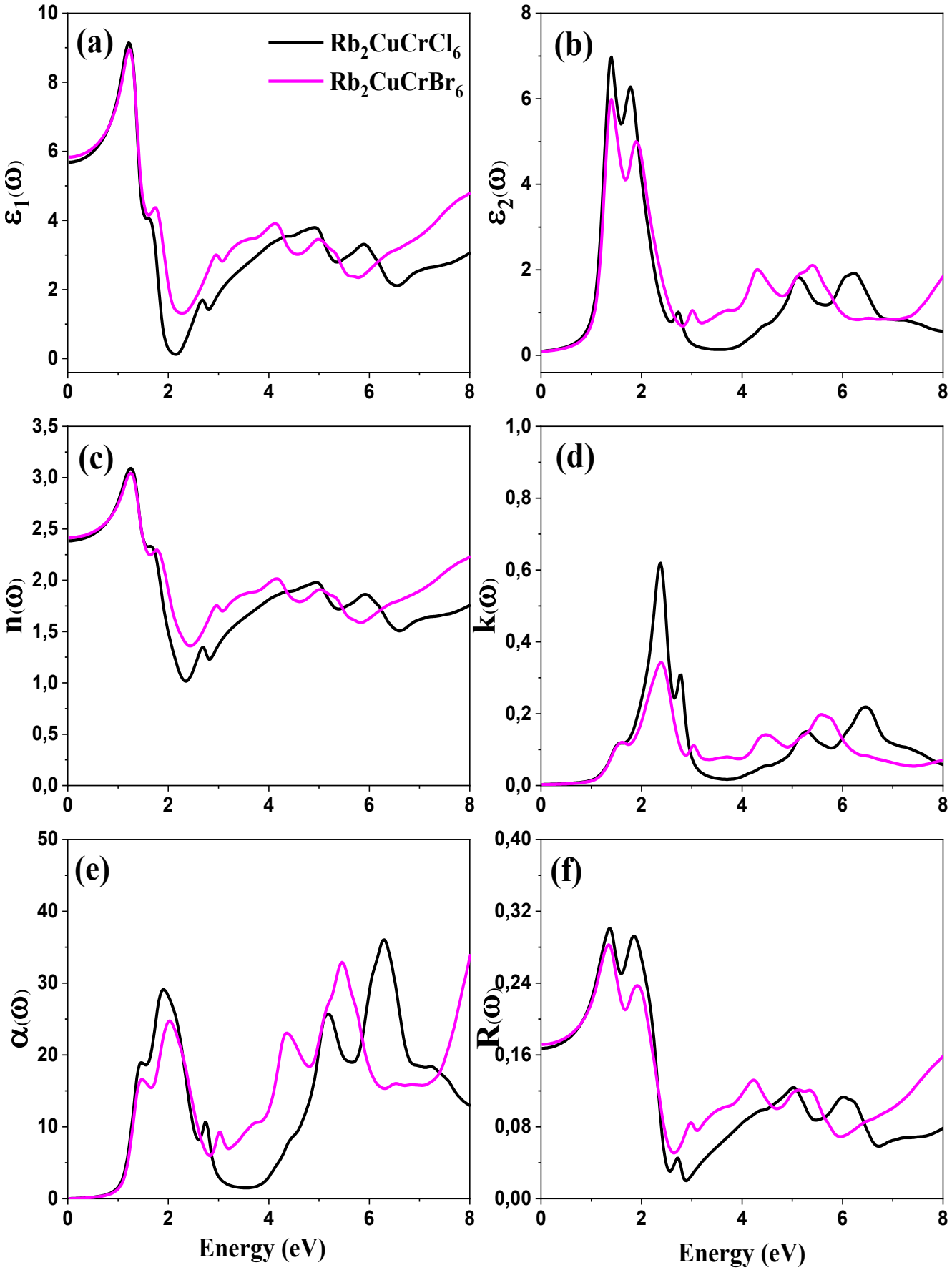

Figure 6. Calculated optical properties of $Rb_2CuCrCl_6$ and $Rb_2CuCrBr_6$ over the energy range 0–8 eV: (a) real part $\varepsilon_1(\omega)$ and (b) imaginary part $\varepsilon_2(\omega)$ of the dielectric function, (c) refractive index $n(\omega)$, (d) extinction coefficient $k(\omega)$, (e) absorption coefficient $\alpha(\omega)$ and (f) reflectivity $R(\omega)$

10.57647/jtap.2026.2004.03

The reflectivity shows a slight increase in the 1–2 eV region, corresponding to the strong interband transitions, but remains below 0.25 even at the peaks.

To evaluate the potential for solar cell applications quantitatively, we compare the absorption characteristics with the Shockley-Queisser limit [52]. While the band gaps (0.88 eV, 0.79 eV) are below the optimal 1.34 eV for single-junction cells, the high absorption coefficients ($\sim 10^5$ cm^{-1}) and broad spectral response make these materials excellent candidates for: (*i*) bottom-cell absorbers in tandem photovoltaic devices, where they would complement wider-band-gap top cells; (*ii*) near-infrared photodetectors operating in the 800–1400 nm range; and (*iii*) thermophotovoltaic systems designed for infrared radiation harvesting.

The absorption coefficient at the peak of the solar spectrum (~2.5 eV) exceeds 5×10^4 cm^{-1} for both compounds, ensuring efficient carrier generation in thin-film architectures.

The optical properties presented here are calculated within the independent particle approximation using TB-mBJ. While this approach captures the main features of the dielectric function, future work incorporating excitonic effects via Bethe-Salpeter equation (BSE) calculations would provide a more complete description, particularly near the absorption edge where electron-hole interactions may enhance the optical response.

3.4. Magnetic properties

In recent decades, both theoretical and experimental studies have increasingly focused on double perovskites for spintronic applications, particularly exploiting phenomena such as tunnel magnetoresistance (TMR) and giant magnetoresistance (GMR). The primary advantage of these materials lies in their enhanced magnetic moments and potentially high Curie temperatures (T_C), properties that are essential for practical magnetic compounds. The magnetic moment of double perovskites (DPs) mostly arises from the incorporation of transition metal ions at the B-sites. These metals possess unpaired d electrons that are the primary source of the material's total magnetic moment. Optimization of the magnetic moment for various applications can be achieved by selecting appropriate transition metal combinations. Exceptionally elevated magnetic moments render these compounds highly appealing for data storage and spintronic devices [59]. The calculated magnetic properties of Rb_2CuCrX_6 (X = Cl, Br) are presented in Table 2. The uniform total magnetic moments, approximately 3 μ_B per formula unit for both compounds, reflect robust magnetic ordering arising from the high-spin state of the Cr^{3+} ions ($3d^3$ configuration). This configuration is stabilized through significant crystal field splitting in an octahedral coordination, with spin alignment following Hund's rule.

Table 2. Computed site-resolved magnetic moments (in μ_B) and total band gap energy E_g (eV) for $Rb_2CuCrCl_6$ and $Rb_2CuCrBr_6$

Compounds	M(Tot)	m(Rb)	m(Cr)	m(Cu)	m(X)	E_g
$Rb_2CuCrCl_6$	3.00	0.00	2.62	0.06	0.03	0.88
$Rb_2CuCrBr_6$	3.00	0.00	2.80	-0.06	0.01	0.79

As discussed in detail above, the site-resolved moments (Table 2) reveal that while Cr carries the majority of the moment (2.62-2.80 μ_B), small induced moments appear on Cu (±0.06 μ_B) and the halogen sites (0.01-0.03 μ_B), demonstrating the role of covalent hybridization in these materials.

The ferromagnetic ground state of Rb_2CuCrX_6 is consistent with recent theoretical work on transition-metal-based perovskites. For instance, Safdar et al. [60] demonstrated that in the $CaCu_3Mn_2Ir_2O_{12}$ system, the lowest energy state (FiM-II) is determined by comparing energy differences of −191.67 meV and −37.47 meV relative to FM and FiM-I configurations. While our study focuses on FM ordering, the robustness of our 3.00 μ_B moment aligns with the site-resolved moments reported in such systems.

The site-resolved moments in our work (Table 2) exhibit features comparable to those reported by Safdar et al. [59] for $CaCu_3Mn_2Ir_2O_{12}$. In their study, Cu carries 0.6 μ_B, Mn carries 3.25 μ_B, and Ir shows a negative moment of -0.57 μ_B, indicating antiparallel alignment. Similarly, our Cr-dominated moments (2.62-2.80 μ_B) with small induced moments on Cu (±0.06 μ_B) and halogens (0.01-0.03 μ_B) reflect the role of hybridization. The negative Cu moment in $Rb_2CuCrBr_6$ suggests weak antiferromagnetic coupling between Cu and the Cr-halogen framework, analogous to the Ir behavior in their FiM-II state. This distribution deviates significantly from the ionic free-ion estimate of 3.87 μ_B for isolated Cr^{3+}, demonstrating the importance of covalent bonding in these materials. The total cell moment of 3.00 μ_B, however, remains consistent with the expected integer value for a high-spin d^3 configuration, confirming that the 'missing' moment is delocalized onto ligand sites through hybridization rather than being quenched.

The origin of the small induced moments on Cu and halogen sites can be understood from the PDOS analysis (Figures 4 and 5). Strong covalent hybridization between Cr-3d and halogen-p orbitals leads to the formation of bonding and antibonding states that have mixed character. Consequently, a small fraction of the spin density from Cr is transferred to the ligand sites.

10.57647/jtap.2026.2004.03

This effect is more pronounced in the Cl compound (m(Cl) = 0.03 μ_B) compared to the Br compound (m(Br) = 0.01 μ_B), which can be attributed to the higher electronegativity and stronger covalent bonding tendency of Cl relative to Br. The negative moment on Cu in $Rb_2CuCrBr_6$ (-0.06 μ_B) indicates a weak antiferromagnetic coupling between Cu and the Cr-halogen framework, a subtle effect that would be entirely missed in an ionic model.

While Safdar et al. [60] achieved 100% spin polarization through half-metallic behavior with a 0.7 eV minority-spin gap, our compounds exhibit semiconducting behavior in both spin channels. This distinction highlights the diversity of spintronic materials: half-metals like $CaCu_3Mn_2Ir_2O_{12}$ offer perfect spin filtering, whereas ferromagnetic semiconductors like Rb_2CuCrX_6 enable gate-tunable spin transport. The robust 3.00 μ_B moment in our systems ensures significant spin polarization even in the absence of half-metallicity.

The double perovskite $Rb_2CuCrCl_6$ comprises copper in the +1 oxidation state (Cu^+), chromium in the +3 oxidation state (Cr^{3+}), and chloride anions (Cl^-). The chromium ion, Cr^{3+}, with three unpaired electrons in its 3d orbitals ($3d^3$ configuration), is the principal contributor to the magnetic moment in this structure, yielding the expected spin-only moment of 3 μ_B. The copper ion, Cu^+, possesses a fully occupied $3d^{10}$ electron shell and therefore has no unpaired electrons in a purely ionic picture. However, as shown in Table 2, a small induced magnetic moment appears on Cu (±0.06 μB), which arises from covalent hybridization with surrounding atoms rather than from intrinsic Cu^{2+} character. These results are consistent with recent studies on K_2CuCrZ_6 and Cs_2CuCrZ_6 [41, 42], which also report Cr-dominated magnetism with small induced moments on Cu, thereby reinforcing the robustness of our findings and the importance of hybridization effects in these systems.

Following the approach of Safdar et al. [60], who estimated a Curie temperature of 322 K for $CaCu_3Mn_2Ir_2O_{12}$ using Heisenberg exchange parameters derived from total energy differences of multiple magnetic configurations, future work on Rb_2CuCrX_6 should include explicit calculations of antiferromagnetic (AFM) states to extract exchange constants and estimate T_C. Such studies would provide deeper insight into the magnetic stability of these materials at finite temperatures.

While explicit exchange constants and Curie temperatures were not calculated in this study, several qualitative indicators suggest robust magnetic ordering. The large exchange splitting observed in the PDOS (Figures 4-5) and the integer total magnetic moment of 3.00 μ_B both indicate strong ferromagnetic coupling. Furthermore, the close chemical and structural similarity to K- and Cs-based analogs [41, 42], which have been reported to exhibit high magnetic stability, supports the expectation that Rb_2CuCrX_6 may possess Curie temperatures above room temperature. Nevertheless, we acknowledge that explicit extraction of exchange parameters and T_C estimation via mean-field or Monte Carlo methods would provide quantitative confirmation and are recommended for future investigations.

4. Conclusion

In conclusion, the cubic phase of the halide perovskites $Rb_2CuCrCl_6$ and $Rb_2CuCrBr_6$ has demonstrated thermodynamic and energetic stability as confirmed by negative formation energies (ΔH_f = -1.07 eV and -1.35 eV, respectively).

While the present work confirms the ferromagnetic ground state through structural optimization and magnetic moment analysis, explicit calculation of antiferromagnetic configurations and subsequent estimation of Curie temperatures via Monte Carlo simulations would provide deeper insight into magnetic stability at finite temperatures. Such investigations are planned for future work.

Band structure calculations using the TB-mBJ potential reveal that both compounds are indirect band gap semiconductors with E_g values of 0.88 eV ($Rb_2CuCrCl_6$) and 0.79 eV ($Rb_2CuCrBr_6$).

The proximity of the Fermi level to the valence band maximum indicates p-type behavior, consistent with the Cu-3d–halogen-p character of the valence band edge.

The magnetic properties arise from a well-defined mechanism rooted in the crystal chemistry. The octahedral coordination of Cr^{3+} produces a crystal field splitting Δ_{CF} of approximately 1–2 eV, stabilizing the high-spin d^3 configuration ($t_{2g}^3\uparrow$, e_g^0) with three unpaired electrons. This configuration yields the spin-only moment of 3 μ_B and provides localized spins for magnetic ordering. Ferromagnetism is mediated by superexchange interactions along Cr–X–Cu–X–Cr pathways, where X = Cl or Br. In this mechanism, Cr 3d and Cu 3d orbitals hybridize with halogen p orbitals, creating an effective ferromagnetic coupling between Cr^{3+} ions. The strength of this interaction is reflected in the large exchange splitting ($\Delta_{ex} \approx$ 2.5–3.0 eV) observed in the PDOS and the robust total magnetic moment of 3.00 μ_B. Halogen substitution modulates the exchange interaction: the more covalent character of Br enhances hybridization, correlating with the slightly larger Cr-projected moment in $Rb_2CuCrBr_6$ (2.80 μ_B) compared to $Rb_2CuCrCl_6$ (2.62 μ_B).

Both compounds demonstrate significant optical absorption from the near-infrared to the ultraviolet, with absorption coefficients reaching 10^4–10^5 cm^{-1}. The dielectric functions $\varepsilon_1(\omega)$ and $\varepsilon_2(\omega)$ indicate high efficiency in light absorption, particularly in the infrared, with $Rb_2CuCrBr_6$ extending absorption into the visible region.

Refractive indices (2.38–2.41) and extinction coefficients confirm substantial light-matter interaction, with maximum absorption in the 2–3 eV range. The low reflectivity (<0.20) ensures that most incident light is absorbed rather than reflected, advantageous for photovoltaic applications.

While the band gaps are below the optimal range for single-junction solar cells, the high absorption coefficients and broad spectral response make these materials excellent candidates for bottom-cell absorbers in tandem devices and near-infrared photodetectors. This integrated analysis demonstrates that the electronic, magnetic, and optical properties of Rb_2CuCrX_6 are not independent but emerge from interconnected structure-property relationships: crystal field splitting determines the Cr spin state, exchange pathways mediated by halide orbitals govern magnetic coupling, and halogen chemistry simultaneously controls the band gap and absorption characteristics. These mechanistic insights provide a rational basis for tuning these materials for specific optoelectronic and spintronic applications. While the present work establishes fundamental properties, further investigations into exchange coupling mechanisms, spin polarization dynamics, and detailed transport behavior would provide deeper insight.

Future work should include benchmark calculations using hybrid functionals or GW methods to validate band gaps, DFT+U calculations to explore correlation effects, and Bethe-Salpeter equation (BSE) calculations to capture excitonic effects in optical spectra."

Acknowledgments

The authors would like to thank the general directorate for scientific research and technological development for their financial support during the realization of this work.

Authors Contribution

All the authors have participated sufficiently in the intellectual content, conception and design of this work or the analysis and interpretation of the data, as well as the writing of the manuscript.

Availability of data and materials

Data will be made available upon reasonable request to the corresponding author.

Conflict of interests

The authors declare no conflict of interest.

References

[1] Waldrop MM. More than Moore. Nature. 2016;530(7589):144-148.

[2] Barla P, Joshi VK, Bhat S. Spintronic devices: a promising alternative to CMOS devices. J Comput Electron. 2021;20(2):805-837.

[3] Warner JH, Schaffel F, Rummeli M, Bachmatiuk A. Graphene: fundamentals and emergent applications. Oxford: Newnes; 2012.

[4] Saha D, Holub M, Bhattacharya P, Basu D. Spin-based semiconductor heterostructure devices. 2011.

[5] Burkard G, Ladd TD, Pan A, Nichol JM, Petta JR. Semiconductor spin qubits. Rev Mod Phys. 2023;95(2):025003.

[6] Wang KL, Alzate JG, Amiri PK. Low-power non-volatile spintronic memory: STT-RAM and beyond. J Phys D Appl Phys. 2013;46(7):074003.

[7] Žutić I, Fabian J, Sarma SD. Spintronics: fundamentals and applications. Rev Mod Phys. 2004;76(2):323.

[8] Inomata K, Ikeda N, Tezuka N, Goto R, Sugimoto S, Wojcik M, et al. Highly spin-polarized materials and devices for spintronics. Sci Technol Adv Mater. 2008;9(1):014101.

[9] Nid-Bahami A, El Kenz A, Benyoussef A, Bahmad L, Hamedoun M, El Moussaoui H. Magnetic properties of double perovskite Sr2RuHoO6: Monte Carlo simulation. J Magn Magn Mater. 2016;417:258-266.

[10] Bensehil I, Baaziz H, Ghellab T, Djeghloul F, Zaiou S, Charifi Z. Unveiling the properties of FrBX3 (B = Pb, Zr; X = Br, Cl) inorganic metal halide perovskites: electronic, optical, and mechanical perspectives. Phys Solid State. 2025;67(10):918-931.

[11] Mouna SC, Radjai M, Bouhemadou A, Houatis D, Allali D, Essaoud SS, et al. Structural, elastic, and thermodynamic properties of BaXCl3 (X = Li, Na) perovskites under pressure effect: ab initio exploration. Phys Scr. 2023;98:065949.

[12] You J, Li G, Zhang S, Zhang X, Luo J, Rao M, et al. Synthesis, characterization and thermodynamic properties of KNbO3. J Alloys Compd. 2021;882:160641.

[13] Mahmood Q, Yaseen M, Hassan M, Rashid MS, Tlili I, Laref A. The first-principle study of mechanical, optoelectronic and thermoelectric properties of CsGeBr3 and CsSnBr3 perovskites. Mater Res

Express. 2019;6:045901.

[14] Behera D, Dixit A, Kumari K, Srivastava A, Sharma R, Mukherjee SK, et al. Structural, elastic, mechanical, and thermodynamic characteristic of NaReO3 and KReO3 perovskite oxides from first principles study. Eur Phys J Plus. 2022;137:1345.

[15] Zheng W, Cheng H, Liu Y, Chen L, Guo Y, Yang Y, et al. Machine learning for imbalanced datasets: application in prediction of 3d-5d double perovskite structures. Comput Mater Sci. 2022;209:111394.

[16] Bhalla AS, Guo R, Roy R. The perovskite structure: a review of its role in ceramic science and technology. Mater Res Innov. 2000;4:3-26.

[17] Chanda S, Maity R, Saha S, Dutta A, Sinha TP. Double perovskite nanostructured Dy2CoMnO6 an efficient visible-light photocatalysts: synthesis and characterization. J Sol-Gel Sci Technol. 2021;99:600-613.

[18] Bhatti IN, Bhatti IN, Mahato RN, Ahsan MAH. Physical properties in nano-crystalline Ho2CoMnO6. Ceram Int. 2020;46:46-55.

[19] Younas M, Mahmood Q, Kattan NA, Alshahrani T, Mera A, Amin MA, et al. Study of new double perovskites Tl2PtX6 (X = Cl, Br, I) for solar cells and thermoelectric applications. Phys Scr. 2022;97:125803.

[20] Ramawat S, Kukreti S, Kale AJ, Dutt R, Chakrabarti A, Dixit A. Cs2KMnCl6: a possible half-metallic double perovskite for spintronics. J Appl Phys. 2023;133.

[21] Aqtash NA, Al Azar SM, Al-Reyahi AY, Mufleh A, Maghrabi M, Essaoud SS, et al. First-principles calculations to investigate structural, mechanical, electronic, optical, and thermoelectric properties of novel cubic double perovskites X2AgBiBr6 (X = Li, Na, K, Rb, Cs) for optoelectronic devices. Mol Simul. 2023;49:1-12.

[22] Djefal A, Amari S, Obodo KO, Beldi L, Bendaoud H, Evans RFL, et al. Half-metallic ferromagnetism in double perovskite Ca2CoMoO6 compound: DFT+U calculations. SPIN. 2017;7:1750009.

[23] Ketfi ME, Essaoud SS, Al Azar SM, Al-Reyahi AY, Mousa AA, Al-Aqtash N. Mechanical, magneto-electronic and thermoelectric properties of Ba2MgReO6 and Ba2YMoO6 based cubic double perovskites: an ab initio study. Phys Scr. 2024;99:015908.

[24] Ammar Yasir M, Saeed U, Noor NA, Mumtaz S, Elhindi KM. Computational strain engineering and Hubbard's effect investigation on Li2CuWX6 (X = Cl, Br) double perovskites: a promising route to spintronic innovation. J Phys Chem Solids. 2025;203:112733.

[25] Khan H, Murtaza G, Shakir MB, Touqir M, Mumtaz S, Azzam MM. Computational investigation of thermodynamic, optoelectronic, and thermoelectric aspects of double perovskites A2YBiO6 (A = Mg, Ca, Ba): promising green energy alternatives. Chem Phys Lett. 2025;868:142057.

[26] Mustafa GM, Younas B, Waseem M, Rehman AA, Noor NA, Elhindi KM, et al. Investigation of optoelectronic and thermoelectric characteristics of Tl2Os(Cl/Br)6 double perovskites for renewable energy applications. Mater Sci Semicond Process. 2025;192:109420.

[27] Nazir S, Noor NA, Majeed F, et al. First-principles calculations of halide double perovskite K2InBiX6 (X = Cl, Br, I) for solar cell applications. J Inorg Organomet Polym Mater. 2025;35:5721-5735.

[28] Chen C, Du Y, Xu Y, Wang Z, Tuo Y, Han Z, et al. Machine learning and first-principles study of non-lead-halogen Cs2NaB'Cl6 (B' = In, Cr, Y, Tb) double halide perovskites with optoelectronic properties. Mater Sci Eng B. 2025;316:118135.

[29] Sofi MY, Khan MS, Khan MA. Structural stability, magneto-electronic behavior, and thermoelectric properties of Cs2AgMBr6 (M = V, Mn, Ni) halide double perovskites: a first-principles study. Mater Sci Semicond Process. 2024;186:109023.

[30] Varadwaj PR. A2AgCrBr6 (A = K, Rb, Cs) and Cs2AgCrX6 (X = Cl, I) double perovskites: a transition-metal-based semiconducting material series with remarkable optics. Nanomaterials. 2020;10(5):973.

[31] Varadwaj PR, Marques HM. Physical and optoelectronic features of lead-free A2AgRhBr6 (A = Cs, Rb, K, Na, Li) with halide double perovskite composition. J Mater Chem C. 2020;8:12968-12983.

[32] Shah S, Ali Z, Mehmood S, Khan I, Ahmad I. Electronic structure, optical and magnetic properties of double perovskites La2MTiO6 (M = Co, Ni, Cu

and Zn). Mater Chem Phys. 2021;272:125050.

[33] Kumari S, Rani U, Rani M, Singh R, Kamlesh PK, Kumari S, et al. Computational investigation of the fundamental physical properties of lead-free halide double perovskite Rb2NaCoX6 (X = Cl, Br, and I) materials: potential prospects for sustainable energy. Mod Phys Lett B. 2024;38(34).

[34] Tirth V, Kamran M, Alrefaee SH, Quraishi AM, Abduvalieva D, Almahri A, et al. Structural, electronic, magnetic, optical and thermoelectric properties of ferromagnetic double perovskites K2ScCoX6 (X = F, Cl): a first-principles study. Case Stud Therm Eng. 2024;64:105433. https://doi.org/10.1016/j.csite.2024.105433

[35] Dar SA, Murtaza G, Zelai T, Nazir G, Alkhaldi H, Albalawi H, et al. Study of structural, electronic, magnetic, and optical properties of A2FeMnO6 (A = Ba, La) double perovskites, experimental and DFT analysis. Colloids Surf A Physicochem Eng Asp. 2023;664:131145-1311415.

[36] Abdullah D, Gupta DC. Exploring the half-metallic ferromagnetism, dynamical and mechanical stability, optoelectronic and thermoelectric properties of K2NaMI6 (M = Mn, Co, Ni) for spintronic applications. Sci Rep. 2023;13(1). https://doi.org/10.1038/s41598-023-39230-2

[37] Khan NU, Khan UA, Zaman A, Algahtani A, Al-Humaidi JY, Tirth V, et al. Insight into structural, electronic, optical and elastic properties of double perovskites Rb2XCrCl6 (X = K, Na) via DFT study. J Phys Chem Solids. 2023;181:111479. https://doi.org/10.1016/j.jpcs.2023.111479

[38] Singh U, Klarbring J, Abrikosov IA, Simak SI. Exploring magnetism of lead-free halide double perovskites: a high-throughput first-principles study. Phys Rev Mater. 2023;7(11):114404.

[39] Berri S, Bouarissa N. First-principles calculations on novel Rb-based halide double perovskites alloys for spintronics and optoelectronic applications. Opt Photonics J. 2024;14:1-22.

[40] Mopoung K, Ning W, Zhang M, Ji F, Mukhuti K, Engelkamp H, et al. Understanding antiferromagnetic coupling in lead-free halide double perovskite semiconductors. J Phys Chem C. 2024;128(10):5313-5320.

[41] Ameer MA, Mustafa GM, Gassoumi A, Saba S, Noor NA, Mumtaz S, et al. Theoretical analysis of magnetic, optoelectronic, and thermoelectric properties of Cs2CuCrX6 (X = Cl and Br) double perovskites for spintronic and data storage devices. J Phys Chem Solids. 2024;193:112149.

[42] Noor NA, Khan MA, Niaz S, Mumtaz S, Nazir S, Elhindi KM. Systematic study of spin dependent electronic, mechanical, optoelectronic and thermoelectric properties of halide double perovskites K2CuCrZ6 (Z = Cl, Br): DFT-calculations. J Phys Chem Solids. 2025;198:112474.

[43] Blaha P, Schwarz K, Madsen GK, Kvasnicka D, Luitz J. WIEN2k: an augmented plane wave plus local orbitals program for calculating crystal properties. Austria: University of Wien; 2001.

[44] Blaha P, Schwarz K, Tran F, Laskowski R, Madsen GK, Marks LD. WIEN2k: an APW+lo program for calculating the properties of solids. J Chem Phys. 2020;152(7):074101-074130.

[45] Tran F, Blaha P. Accurate band gaps of semiconductors and insulators with a semilocal exchange-correlation potential. Phys Rev Lett. 2009;102(22):226401-226404.

[46] Koller D, Tran F, Blaha P. Improving the modified Becke-Johnson exchange potential. Phys Rev B. 2012;85(15):155109.

[47] Koller D, Tran F, Blaha P. Merits and limits of the modified Becke-Johnson exchange potential. Phys Rev B. 2011;83(19):195134-195210.

[48] Murnaghan FD. Proc Natl Acad Sci U S A. 1944;30:244.

[49] Khan MU, Rahman AU, Ahmad M, Yaseen M, Ahmed MA. Exploring room-temperature ferromagnetism and half-metallicity in new halide perovskites RbCrX (X: F, Cl, Br, I) using first-principles and Monte Carlo simulations. Eur Phys J Plus. 2024;139:106.

[50] Noor NA, Khan MA, Niaz S, Mumtaz S, Nazir S, Elhindi KM. Systematic study of spin dependent electronic, mechanical, optoelectronic and thermoelectric properties of halide double perovskites K2CuCrZ6 (Z = Cl, Br): DFT-calculations. J Phys Chem Solids. 2025;198:112474.

[51] Goldschmidt VM. Die Gesetze der Krystallochemie. Naturwissenschaften. 1926;14(21):477-485.

[52] Shockley W, Queisser HJ. Detailed balance limit of efficiency of p-n junction solar cells. J Appl Phys. 1961;32:510. https://doi.org/10.1063/1.1736034

[53] Murtaza G, Ahmad I. First principle study of the structural and optoelectronic properties of cubic perovskites CsPbM3 (M = Cl, Br, I). Physica B. 2011;406(17):3222-3229.

[54] Abbas S, Najar FA, Samad R, Sultan K. The electronic and optical behavior of anisotropic Nd2NiMnO6 double perovskite: a first principle study. Solid State Commun. 2021;338:114463.

[55] Bensehil I, Baaziz H, Ghellab T, Djeghloul F, Zaiou S, Kolli A, et al. Investigating the structural, electronic, magnetic, mechanical, anisotropic and optical aspects of CoFeYSb (Y = V and Ti) quaternary Heusler alloys from first principles. J Supercond Nov Magn. 2025;38(59).

[56] Ravichandran R, Wang AX, Wager JF. Solid state dielectric screening versus band gap trends and implications. Opt Mater. 2016;60:181-187.

[57] Dong Y, Zhu R, Jia Y. Linear relationship between the dielectric constant and band gap in low-dimensional mixed-halide perovskites. J Phys Chem C. 2021;125(27):14883-14890.

[58] Forouhi AR, Bloomer I. Optical properties of crystalline semiconductors and dielectrics. Phys Rev B. 1988;38(3):1865-1874.

[59] Pei L, Jiang JJ, Ma XG, Tian B. Nature of magnetic and electronic structure of double perovskite A2FeMoO6. Trans Nonferrous Met Soc China. 2007;17(7):1661-1666.

[60] Safdar, et al. Physica B Condens Matter. 2025;707:417149. https://doi.org/10.1016/j.physb.2025.417149